ECLÉTICA QUÍMICA

Eclet. Quim. 51 | e-1506, 2026

Original Articles in Chemistry and Related Areas

https://doi.org/10.26850/1678-4618.eq.v51.2026.e1506

Pyrazinamide-derived hydrazone outperforms pyrazinamide activity in *Mycobacterium tuberculosis* DM97: an *in vitro* and *in silico* study

Christian Aliaga **Paucar**[1], Jesús **Alvarado-Huayhuaz**[1], Henrry Gutierrez **Vega**[1], Ramirez Panti **Rocio**[1], Mirko Zimic **Peralta**[2], Patricia Sheen **Cortavarria**[2], Ana Valderrama **Negrón**[1+]

Abstract

Tuberculosis is an infectious disease caused by *Mycobacterium tuberculosis* (MTB). Pyrazinamide (PZA) is a prodrug used in first-lines treatment. New drugs proposals are urgent, given the increased resistance to antimicrobials such as PZA. In this work, we have synthesized and characterized *N*'-[(1*E*)-(4-nitrophenyl)methylidene]pyrazine-2-carbohydrazide (C3), to evaluate its antituberculosis activity *in vitro* in MTB H37Rv (wild type) and DM97 (PZA resistant). C3 was synthesized and characterized by FT-IR and ^{1}H / ^{13}C NMR, among others. C3 is a hydrazone derived from PZA. Both compounds have an analogous and stable docking with the pyrazinamidase enzyme, according to our *in-silico* studies. In the tetrazolium microplate assay (TEMA) performed on MTB H37Rv at pH 6.0 and 6.8, it was found that PZA has greater antituberculosis activity than C3 on H37Rv, however, in DM97, C3 (MIC = 128 µg / mL at pH 6.0) presented greater antituberculosis activity than PZA (MIC > 800 µg / mL at pH 6.0), which demonstrates the antituberculosis potential of C3 against this strain resistant to PZA.

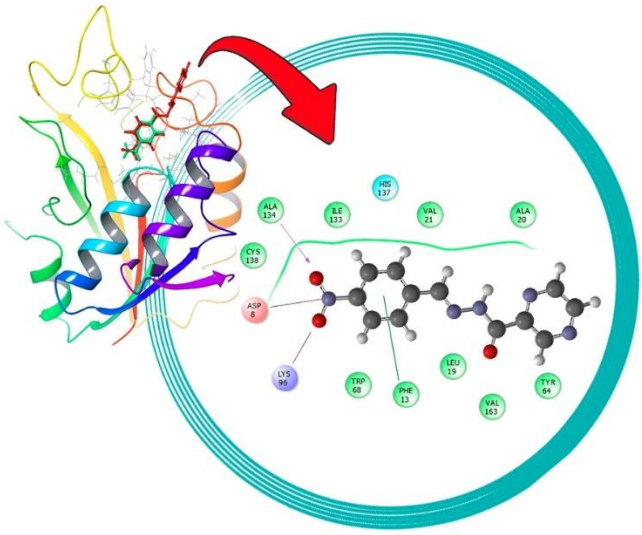

Article History

Received	August 02, 2023
Accepted	July 14, 2025
Published	June 03, 2026

Keywords

1. antimicrobial resistance;
2. antitubercular agents;
3. schiff base;
4. TEMA.

Section Editors

María Natalia Besil **Arismendi**

Highlights

- Molecular docking/molecular dynamics studies of hydrazone targeting pyrazinamidase.
- Evaluation of hydrazone efficacy against *Mycobacterium tuberculosis*.
- Hydrazone shows an inhibitory concentration (MIC) of 128 µg/mL against DM97 strains.
- Hydrazone is more active antituberculosis than PZA against the DM97 strain.

[1]National University of Engineering, Faculty of Science, Lima, Peru. [2]Cayetano Heredia University, Faculty of Science and Philosophy, Lima, Peru.
+Corresponding author: Ana Valderrama Negrón, **Phone:** +51 999934007, **Email address:** ana.valderrama.n@uni.edu.pe

https://doi.org/10.26850/1678-4618.eq.v51.2026.e1506

1. Introduction

Tuberculosis (TB) is an infection caused by *Mycobacterium tuberculosis* (MTB). According to the World Health Organization global TB report of 2023 (WHO, 2023), the number of people treated for TB has increased from 10.3 million in 2021 to 10.6 million in 2022. Approximately 1.3 million people suffering from TB around the world died in 2022. TB is considered the most dangerous infectious disease in the world (WHO, 2023). One cause of the increase in TB cases has been the appearance of multidrug-resistant tuberculosis (MDR-TB) and extremely drug-resistant tuberculosis (XDR-TB), leaving many patients with no other treatment options (Kardan-Yamchi *et al.*, 2020). According to the Ministry of Health of Peru, in 2019, 23,282 cases of TB morbidity were reported, along with 20,546 new cases of TB, 1,147 new cases of MDR-TB, and 76 new cases of XDR-TB (MINSA, 2019). Pyrazinamide (PZA) is a prodrug and structural analogue of nicotinamide, used as a first-line treatment for tuberculosis (TB) due to its excellent sterilizing effect on tubercle bacilli in a semi-dormant or latent state (Zhang *et al.*, 2003). It is known that PZA is converted to its active form, pyrazinoic acid (POA), by the action of the enzyme pyrazinamidase (PZase) (Sun *et al.*, 2020).

However, the mechanism of action and resistance to PZA is not completely elucidated (Zhang *et al.*, 2003). Many mutations have been documented in the *pncA* gene, which is responsible for the synthesis of PZase, and is likely the primary reason for resistance to PZA (Srivastava *et al.*, 2019). However, there are also strains without mutations in the PZase enzyme that show resistance to PZA, as is the case with MTB DM97 (Carrasco *et al.*, 2021; Chávez *et al.*, 2020; Singh *et al.*, 2006; Valderrama Negrón *et al.*, 2021).

Schiff hydrazone bases (-CH-N-NH-C=O-) have attracted special attention from researchers in recent years due to their well-known chelation capacity (Hegde *et al.*, 2019) and structural flexibility (Shebl *et al.*, 2020), as well as their biological (Zülfikaroğlu *et al.*, 2020) and pharmacological (Shebl, 2017) activities in some diseases, including tuberculosis (Dogan *et al.*, 2020).

Considering the high resistance to PZA that exists in the treatment of TB, there is a need to evaluate new drugs against the latent state of MTB. In the present work, we synthesized and characterized, *N*′-[(1*E*)-(4-nitrophenyl)methylidene]pyrazine-2-carbohydrazide (C3), a PZA derivative covalently linked to a hydrazone group. *In silico* studies were carried out to compare the reactivity of C3 and PZA, and to evaluate their affinity and mode of docking in the PZase enzyme, while *in vitro* studies against MTB H37Rv and MD97 were developed to evaluate their activity in MTB sensitive and resistant to pyrazinamide, respectively. C3 was synthesized and its antituberculosis activity was evaluated for sensitive strains H37Rv (ATCC 27294) by Vergara *et al.* (2009), but no biological tests were performed with resistant strains (DM97).

2. Experimental

All chemicals were purchased from Sigma-Aldrich. The solvents were spectroscopic grade. Melting points were determined with the Thermo Fisher Scientific IA9100 kit. Elemental analysis was determined using a EAI Exetr Analytical CE-440 elemental analyzer. Electronic spectra were recorded using a Shimadzu UV1800 UV-Vis spectrophotometer with a 1 cm quartz cell at room temperature, in the range of 200-400 nm. Infrared spectra were recorded with KBr pellets in the 4000 to 400 cm^{-1} range on a Shimadzu FT-IR Prestige 21 spectrophotometer. ^{1}H-NMR and ^{13}C-NMR spectrum were obtained using a Bruker Ascend 500 MHz spectrometer in DMSO-d_6 with tetramethylsilane (TMS) as an internal standard.

2.1. Procedure for the synthesis of pyrazin-2-carbohydrazide (2)

Hydrazine monohydrate (1.77 mL, 1.81 g, 36.2 mmol) was added to a 5 mL ethanolic solution of methyl pyrazin-2-carboxylate (1) (0.5 g, 3.62 mmol). The mixture was stirred for 2 h at room temperature. The solvent was removed under reduced pressure, and the residue was purified by washing cold Et_2O (20 mL) to afford the product (2) as a solid. This synthesis methodology was reported by Vergara *et al.* (2009).

Yellow solid. 85% yield. Melting point 158-159 °C. IR (KBr): 3382, 3087, 3060, 1718, 1638, 1262 cm^{-1}. ^{1}H-NMR (500 MHz, DMSO-d_6) δ(ppm): 4.56 (s, 2H, NH_2); 8.69 (dd, 1H, J = 1.5 and 2.6 Hz, H-5); 8.82 (d, 1H, J = 2.6 Hz, H-6); 9.12 (d, 1H, J = 1.5 Hz, H-3); 10.11 (s, 1H, CONH). ^{13}C-NMR (126 MHz, DMSO-d_6) δ(ppm): 143.7 (C-5); 144.0 (C-3); 145.4 (C-2); 147.8 (C-6); 162.0 (CONH).

2.2. Procedure for the synthesis of *N*′-[(1*E*)-(4-nitrophenyl)methylidene]pyrazine-2-carbohydrazide (C3)

Pyrazine-2-carbohydrazide (1) (0.138 g, 1 mmol) was dissolved in 10 mL of ethanol. Then, 5 mL of an ethanolic solution of 4-nitrobenzaldehyde (0.151 g, 0.1 mmol) and 4 drops of 6 mol/L H_2SO_4 were slowly added, and the mixture was heated at 40 °C for 2 h. Afterwards, it was allowed to cool until the precipitation of an insoluble solid (C3, **Fig. 1**), then it was filtered, washed with ethanol and recrystallized with DMF, as already reported Vergara *et al.* (2009).

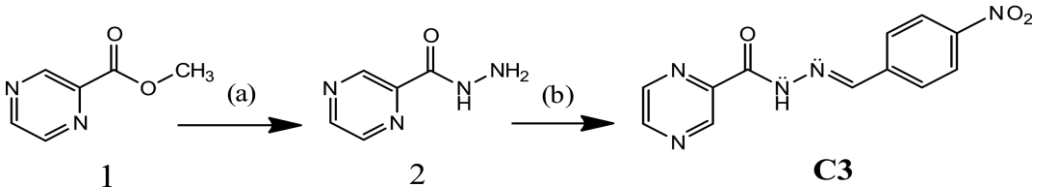

Figure 1. Synthesis conditions; **(a)** Hydrazine monohydrate (98%), EtOH and **(b)** 4-nitrobenzaldehyde, EtOH, H_2SO_4 (6 M).
Source: Elaborated by the authors.

Yellow solid. 92% yield. Melting point 260-261 °C. IR (KBr): 3289, 3028, 1695, 1614, 1579, 1525, 1503, 1336, 1266, 1143 cm^{-1}. ^{1}H-NMR (500 MHz, DMSO-d_6) δ (ppm): 7.98 (d, 2H, J = 8.8 Hz, H-2' and H-6'); 8.31 (d, 2H, J = 8.8 Hz, H-3' and H-5'); 8.76 (s, 1H, N=CH); 8.81 (dd, 1H, J = 2.5 Hz and 1.5 Hz, H-5); 8.95 (d, 1H, J = 2.5 Hz, H-6); 9.29 (s, 1H, J = 1.5 Hz, H-3); 12.6 (s, 1H, CONH). ^{13}C-NMR (126 MHz, DMSO-d_6) δ(ppm): 124.60 (C-3', C-5'); 128.70 (C-2', C-6'); 140.84 (C-1'); 143.90 (C-6); 144.75 (C-2); 144.84 (C-3); 147.86 (C-5); 148.51 (4'); 148.54 (H-C=N); 160.38 (C=O). Anal. Cal: $C_{12}H_9N_5O_3$ (271.23 g/mol): C, 53.14; H, 3.34; N, 25.82. Found: C, 53.18; H, 3.31; N, 25.89.

2.3. *In silico* studies

Computational simulations, also known as *in silico* simulations, enable us to study the interaction between a ligand (PZA or C3) and its receptor, PZase. This approach allows us to analyze the similarities and differences in the ligand-receptor interaction. With this objective, we divide this section into 3 parts: the molecular optimization of ligands, the coupling of these to the pharmacological target and the molecular dynamics simulation, which we detail below.

2.3.1. Quantum mechanical calculations

Quantum mechanics is a powerful tool for the structural optimization of molecules and the study of chemical reactivity. The input for this stage was prepared using Avogadro 1.1.1 (Hanwell *et al.*, 2012) and MarvinSketch 16.2.8, to model the most abundant C3 species at neutral pH (**Fig. S1 - Supplementary Information**). C3 structural optimization, the calculation of its vibrational frequencies, its molecular orbitals, and its electrostatic potential maps (MEP) were generated using the Density Functional Theory (DFT), with the hybrid functional B3LYP and 6-31G* base (Lee *et al.*, 1988) in **ORCA** 4.1.2 software (Neese, 2018). These calculations were made on the Manati supercomputer of the Amazon Research Institute (IIAP, 2020). The highest-energy occupied orbital (HOMO) and the lowest-energy unoccupied orbital (LUMO), or frontier orbitals, were visualized with Avogadro 1.1.1. and the MEPs with Gabedit 2.5.0 (Allouche, 2011).

2.3.2. Molecular docking studies

DFT-optimized structures were saved in SDF format and processed with LigPrep from the Schrödinger Suite 2020.3 (Schrödinger, 2020). The PZase protein was obtained from the Protein Data Bank (PDB ID 3PL1; 2.2 Å) (Petrella *et al.*, 2020). Ions (except iron) and waters of crystallization of the protein were eliminated, and the necessary hydrogens were added at pH 7.4 using PROPKA from the Protein Preparation Wizard module.

The enzymatic activity of PZase depends on Fe^{2+} and its coordination sphere (Asp49, His51, His57, His71 and two water molecules). Therefore, it would be expected to perform the docking considering all the coordinated bonds, including water. However, we need to analyze the interaction of the PZA ligand at the catalytic site, and according to the mechanisms already reported, the exchange of water by PZA is necessary (Sheen *et al.*, 2013). Since the molecular docking technique does not consider the formation or breaking of chemical bonds, we consider eliminating the water molecules and considering the score associated with the interaction with the metal for both PZA and C3. The catalytic site (Asp8, Lys96 and Cys138), the substrate binding residues (Trp68 and Phe13) and the iron atom is coordinated with Asp49, His51, His57, His71 and a water molecule (distance = 2.26 Å). BIOVIA Discovery Studio 2020 was used to create the cubic docking box with an edge of 25 Å and a centroid of coordinates x = 7.34, y = –28.80, z = 1.55 (**D. Systèmes, "BIOVIA." San Diego, 2020**). An initial docking with Glide in standard precision mode (Glide-SP) and an extra precision docking (Glide-XP) were considered, to obtain the affinity energy, applying the potential force field optimized for liquid simulations (OPLS_2005). The analysis of non-covalent interactions was performed with the Ligand Interaction Diagram module of the Schrödinger suite for the 2D visualization of amino acids at distances less than 4 Å from the ligand. It is worth emphasizing that although other studies have already reported the affinity energies of pyrazinamide with the native or mutated PZase protein by molecular docking studies, experimentally, only an APO structure of the protein is available. Therefore, we do not have a ligand co-crystallized with the protein with which we can validate the molecular docking by comparison with the crystallized structure (Alvarado-Huayhuaz *et al.*, 2022).

2.3.3. Molecular dynamics simulations (MDS)

Molecular dynamics simulations were performed to analyze the evolution of intermolecular interactions in ligand-PZase complexes. For this, the results of the molecular docking were used as input files for the MDS, utilizing the System Builder tool within the Schrödinger Suite 2020.3. In addition to the protein, Fe^{2+} and the ligand, about 6000 water molecules were added using TIP3P (Jorgensen *et al.*, 1983) solvation model. With 31 sodium ions and 17 chloride ions, a neutral system was obtained at a physiological salt concentration of 150 mmol/L. Each complex was solvated in periodic boundary conditions (PBC) within an orthorhombic box, 10 Å away from the box edge of the protein, with a total volume of 224920 $Å^3$. Minimization and equilibration were performed in a stepwise manner before the production simulation. After system relaxation, production simulation was performed in the NPT ensemble for 10 ns, using a Reversible Reference System Propagation Algorithm (RESPA) integrator. The system used isothermal-isochoric and isobaric-isothermal assemblies at a temperature of 310.0 K, with the Nosé-Hoover thermostat and a pressure of 1.01325 bar, as implemented in the Martyna-Tobias barostat-Klein within the Desmond 2018-4 software (Bowers *et al.*, 2006). The production phase was carried out on the Heimdall supercomputer at the Institute of Chemistry of the University of São Paulo, Brazil. While this time is not long enough to conclude that the interactions are relatively stable, it does allow us to make an initial assessment of how the coupling obtained by molecular docking evolves in terms of Root Mean Square Deviation (RMSD), Root Mean Square Fluctuation (RMSF), and fraction of interactions.

2.4. Antimicrobial evaluation

The pyrazinamide (PZA) susceptibility test of MTB H37Rv and DM97 strains was performed in a Biosafety laboratory level III using the Tetrazolium Microplate Assay (TEMA) for Cell Viability (3-(4,5-dimethylthiazol-2-yl)-2,5diphenyl-tetrazolium bromide) (Aldrich Chemical Co., Milwaukee, Wis.), which is based in the color change from yellow to blue by the reduction of tetrazolium bromide in viable cells (Benov, 2019; Liu *et al.*, 2002). Using this technique, the minimum inhibitory concentration (MIC) of the drugs was determined in triplicate at pH 6.0 and 6.8. PZA and C3 solutions were sterilized by filtration (0.22 µm) and mixed with 7H9 medium. Controls were non-treated MTB cultures. For the inoculum, the MTB suspension was prepared from a primary culture grown in 7H10 agar medium, which had been previously incubated for 3-4 weeks. The bacterial mass was harvested in a glass tube containing 100 µL of 10% Tween 80 and 3 mm diameter glass beads. After vortex homogenization, the turbidity was adjusted to the McFarland #1 scale (3×10^8 CFU/mL) using 7H9 medium. Finally, the McFarland #1 strain was diluted 1:25 in 7H9 medium. For each well, 100 µL of 1:25 MTB suspension was transferred. The microplates were placed in Ziploc bags and incubated at 37 °C for 6 days for the culture at pH 6.8 and 10 days for the culture al pH 6. Fifty microliters of Tetrazolium were added to a control well. The plates were reincubated at 37 °C for 24 h. If the control well turned blue, the reagent mixture was added to all wells in the microplate. The

microplates we incubated for an additional 24 h at 37 °C, and the colours of all wells were recorded.

The composition and pH of the TEMA medium are crucial for accurately assessing the activity of PZA and related compounds. PZA exhibits pH-dependent activity, showing increased efficacy under mildly acidic conditions (typically around pH 5.5–6.0). This is because its active metabolite, POA, must be protonated in the extracellular space to re-enter the mycobacterial cytosol and induce acidification. This process contributes to its bactericidal mechanism. This intracellular acidification, combined with POA's interaction with essential targets such as RpsA, leads to bacterial death. Therefore, performing the assay at acidic pH ensures the physiological relevance of the results and reflects the true susceptibility profile of the strains tested (Zhang *et al.*, 2014).

3. Results and discussion

3.1. Spectroscopic studies

Compound C3 was obtained by the condensation of pyrazine-2-carbohydrazide with 4-nitrobenzaldehyde. It is soluble in dimethylsulfoxide (DMSO) and dimethylformamide (DMF), but insoluble in polar solvents such as water, methanol, and ethanol.

The UV-Vis absorption spectrum of compound C3 presents two absorption bands. The first, around 266 nm ($\pi \rightarrow \pi^*$ transition), corresponds to the excitation of the electrons of the carbonyl group (C=O) and the aromatic ring of pyrazine (C=N). The second peak around 326 nm (transition $n \rightarrow \pi^*$) corresponds to the excitation of the non-bonding electrons of the O atom (carbonyl group) and N atom (ring pyrazine). The signal of this last transition extends to around 390 nm, due to the presence of the $n \rightarrow \pi^*$ transition of the hydrazone group (-NN=C-) (Bhaskar *et al.*, 2019; Valderrama Negrón *et al.*, 2021).

The FT-IR spectrum displays the vibrational frequencies of the functional groups in compound C3. The N-H stretch is observed as a narrow peak of medium intensity at 3289 cm^{-1}. The carbonyl group has a sharp and narrow peak at 1695 cm^{-1}. The formation of the hydrazone group is evidenced by the stretch of C=N with a moderate intensity at 1614 cm^{-1}. The nitro group presents two characteristic high-intensity signals at 1503 and 1336 cm^{-1}. These results agree with those previously reported in the literature (Vergara *et al.*, 2009).

The ^{1}H resonances of compound C3 are observed in the low-field region of the NMR spectrum, in the range of 7 to 13 ppm (**Fig. 2S in Supplementary Information**). The proton resonance of the hydrazone group (CONH) appears at higher chemical shifts (δ = 12.60 ppm, 1H). A singlet was observed because it does not have close hydrogen atoms to couple with (Silva *et al.*, 2010). This characteristic signal of the proton of the hydrazone group is related to the results obtained by Abdel-Aziz and Abdel-Rahman (2010) for compounds derived from pyrazinamide. The careful analysis of the ^{1}H-NMR spectra of compound C3 indicated the diastereoselectivity of the condensation step as depicted by the presence of only one imino-hydrogen (N=CH) signal for the *N*-acylhydrazone derivative (δ = 8.76 ppm, 1H), which was attributed to the (*E*)-diastereomer. (Silva *et al.*, 2010). Furthermore, it is important to mention that this type of *N*-acylhydrazone derivative has greater stability when forming the (*E*)-diastereomer (Wang, 2020). These characteristic signals of the ^{1}H-NMR spectrum of the *N*-acylhydrazone are related to the results obtained by Silva *et al.* (2010).

In the ^{13}C-NMR spectrum of compound C3 (**Fig. 3S in Supplementary Information**), 10 signals are seen corresponding to the 12 carbons since C-2' and C-6', as well as C-3' and C-5' are equivalent carbon atoms (Ferreira *et al.*, 2010). The carbon that appears in the lower field (δ = 160.38 ppm) is from the carbonyl group (C=O) (Vergara *et al.*, 2009). The signals from C-4' and CH=N have the same displacement; however, when expanding, we can differentiate both signals, where the carbon of CH=N (δ = 148.54 ppm) appears slightly downfield relative to C-4' (δ = 148.51 ppm).

3.2. *In silico* studies

3.2.1. Quantum mechanical calculations

The optimized molecular structures of PZA and C3 are shown in **Fig. 2**. All calculated vibrational frequencies are positive, which indicates a minimum energy conformation. It is observed that the most stable structure of C3 is its *syn* conformation. The frontier molecular orbitals in PZA are distributed throughout the molecule, unlike HOMO in C3, where the pyrazine group is not covered. The calculated energies of HOMO, LUMO and Energy gap were –6.700; –1.726 and 4.974 eV for PZA, while –6.528; –2.760 and 3.768 eV for C3, respectively.

The frontier orbitals of PZA spans the entire molecule. In C3, HOMO does not cover pyrazine, while LUMO does. This greater spatial distribution is reflected in a more stabilized LUMO-C3 orbital (–2.760 eV) compared to the LUMO-PZA orbital (–1.726 eV). As the electronic HOMO-LUMO transition of C3 requires less energy, this compound has greater intrinsic chemical reactivity than PZA (Tariq *et al.*, 2020). MEP of PZA shows us slightly polarized regions, unlike C3, where the nitrate and pyrazine group have high electron density (red), while in a single hydrogen, we identify its opposite (intense blue).

On the other hand, according to physicochemical descriptors obtained from the swissadme.ch website (Daina *et al.*, 2017), it was found that C3 has slightly greater lipophilicity, polarity and flexibility than PZA and is also within the recommended range to be considered as orally bioavailable (**Fig. 4S in Supplementary Information**), which is important to continue to a next stage of studies.

3.2.2. Molecular docking

For the Glide-SP docking stage, –25.75 and –20.05 kJ/mol were obtained for PZA and C3, respectively. For the docking with Glide-XP, –19.80 and –18.96 kJ/mol were obtained for PZA and C3, respectively. Thus, as shown in **Fig. 3**, these ligands overlap in their poses, interacting with the amino acids of the catalytic triad. Hydrogen bonds (H-bonds), lipophilic interactions, and π-π stacking are predominant at the active site.

3.2.3. Molecular dynamics simulations

In **Fig. 4a**, the RMSD ranges from 1.0 to 1.4 Å for PZA and 1.6 to 2.3 Å for the PZase backbone from the second half of the simulation. Such convergence indicates that the PZA-PZase complex is stabilized (Junaid *et al.*, 2019). In **Fig. 4b**, the C3-PZase complex achieves stability after 1 ns of simulation. This analysis suggests that PZA and C3 remain bound to the active site of PZase under the specified simulation conditions.

https://doi.org/10.26850/1678-4618.eq.v51.2026.e1506

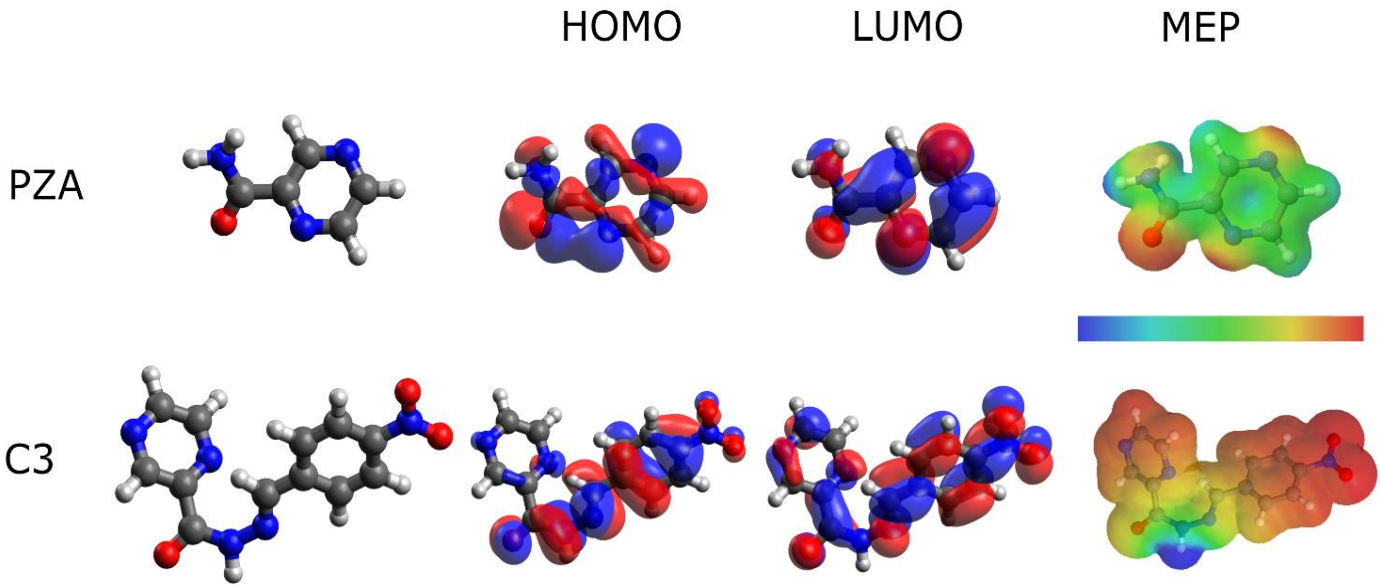

Figure 2. Optimized molecular structures of PZA and C3, HOMO and LUMO frontier molecular orbitals, and electrostatic potential maps (MEP). Colour notation on atoms: black, white, red, and blue, for carbon, hydrogen, oxygen, and nitrogen, respectively. Colour notation on the electrostatic potential map: from red to blue, regions in space from high to low electron density.
Source: Elaborated by the authors.

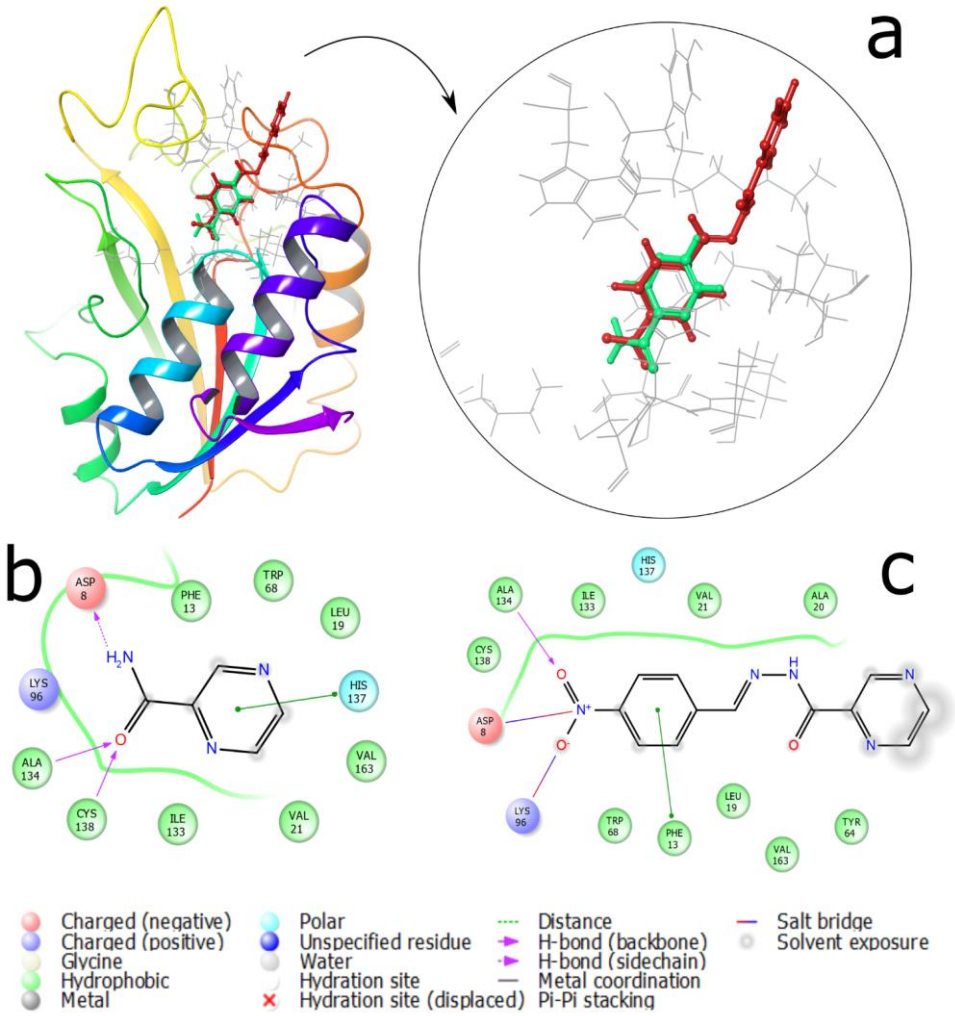

Figure 3. (a) Overlay of PZA (green) and C3 (red) docked to PZase. 2D amino acid interaction diagram with **(b)** PZA and **(c)** C3.
Source: Elaborated by the authors.

https://doi.org/10.26850/1678-4618.eq.v51.2026.e1506

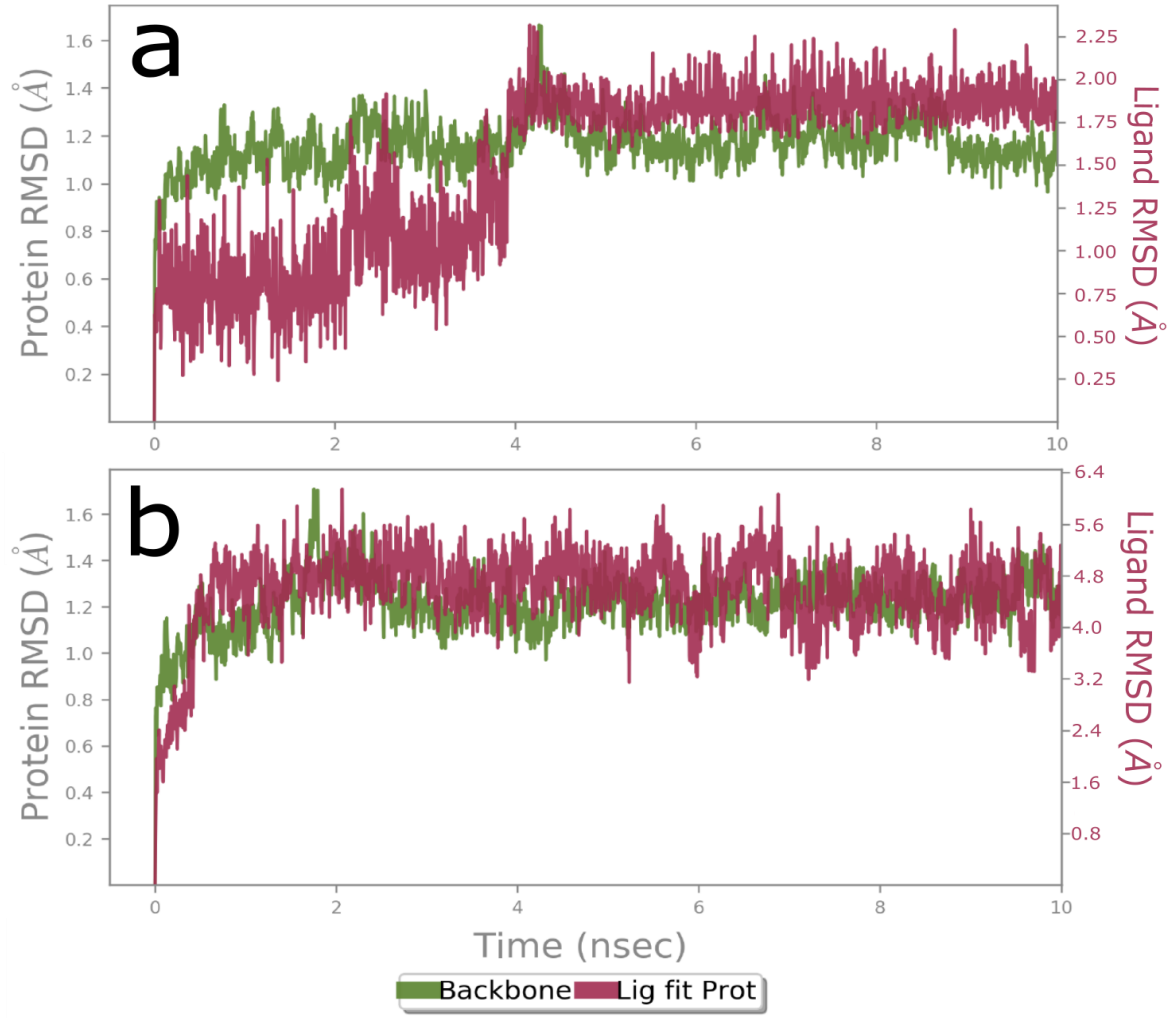

Figure 4. RMSD of the PZase backbone (green line) and ligand in the protein (maroon line) during 10 ns of molecular dynamics simulation for **(a)** PZA and **(b)** C3.
Source: Elaborated by the authors.

In **Fig. 5**, it is observed that all the amino acids in contact with the PZA or C3 (vertical lines) present fluctuations lower than 1 Å. In general, all the amino acid distances of the protein do not exceed 2.3 or 2.5 Å for PZA or C3, respectively, which would indicate that these amino acids do not undergo significant structural changes (Supo-Escalante *et al.*, 2020).

PZA interacts by H-bonds with Cys138 (**Fig. 6a**) throughout the simulation. This same interaction (green bar) occurs with Asp8, Ile133 and Ala134 for more than 4 ns. Lipophilic interactions (pink bar) predominate mainly with Phe13 and Trp68. We emphasize that water is explicitly identified in the active site through H-bonds interactions (blue bar), which would allow a catalytic reaction not contemplated by docking tests. In **Fig. 6b**, Cys138 interacts via an H-bond (green bar) with C3 for less than 2 ns, with Ala20 becoming relevant in this type of interaction. Ser18, Ala20, Tyr64 and Val163 give indications of the participation of water bridges, which could favour a probable catalytic reaction with C3. Trp68 lipophilic interactions occur with more than one atom of C3, which is shown by the pink bar as an interaction fraction greater than 100%. According to the results shown, we can interpret that C3 has a strong affinity for interacting with the amino acids of the active site, including the catalytic amino acids, and could have favourable conditions for chemical reaction (Zhang *et al.*, 2014).

The use of both a pyrazinamide-susceptible (H37Rv) and a pyrazinamide-resistant (DM97) strain allowed for a comparative functional analysis of wild-type and mutated PZase activity. While our molecular modeling studies were based on the wild-type enzyme structure (PDB: 3PL1), the differential MIC results observed experimentally provide indirect evidence of the impact of the T135P mutation. In H37Rv, both PZA and C3 were active, though PZA was more potent. In contrast, in DM97, only C3 retained significant activity, suggesting that its mechanism of action is independent of enzymatic activation by PZase. These findings support the potential of hydrazone derivatives such as C3 as candidates for overcoming pyrazinamidase-mediated resistance.

3.3. Antimicrobial evaluation

According to the TEMA results (**Fig. 7**), the MIC of PZA decreases from 100 to 3.125 µg/mL when the pH decreases from 6.8 to 6.0 for both H37Rv and WT, while for DM97 it remains at values above 800 µg/mL. On the other hand, for C3 in WT at pH 6 and pH 6.8, the MIC remains at concentrations above 256 µg/mL; while for DM97, the MIC decreases from a value above 256 to 128 µg/mL.

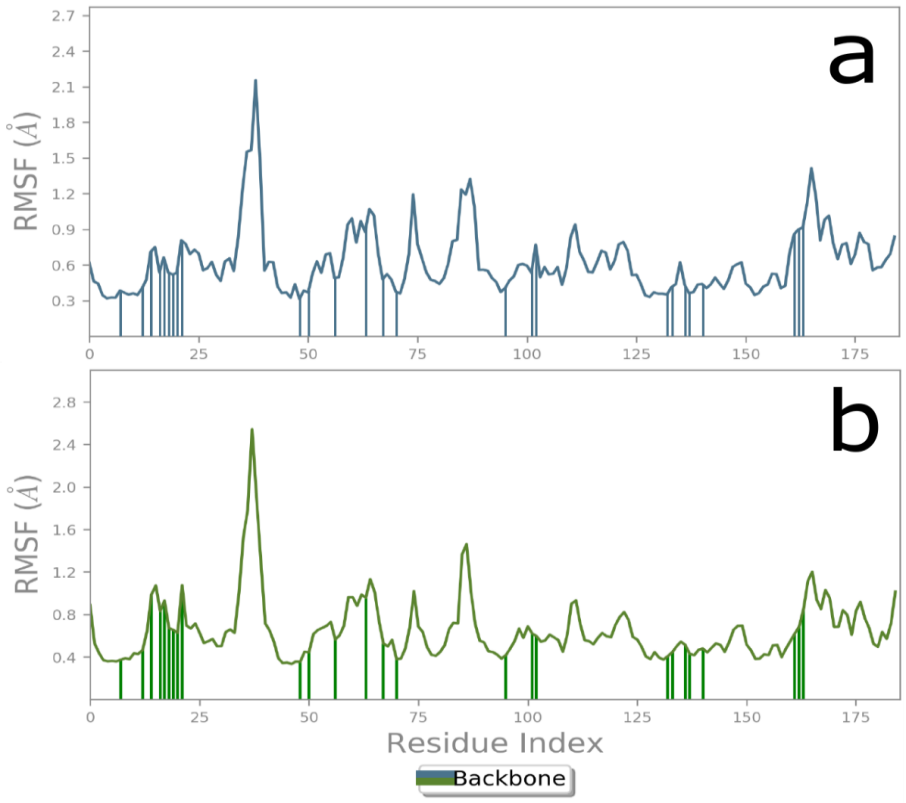

Figure 5. Residue index versus RMSF of the backbone (blue or green line) during 10 ns of molecular dynamics simulation of **(a)** PZA and **(b)** C3. Vertical lines under the RMSF curve indicate amino acids that directly interact with ligands.
Source: Elaborated by the authors.

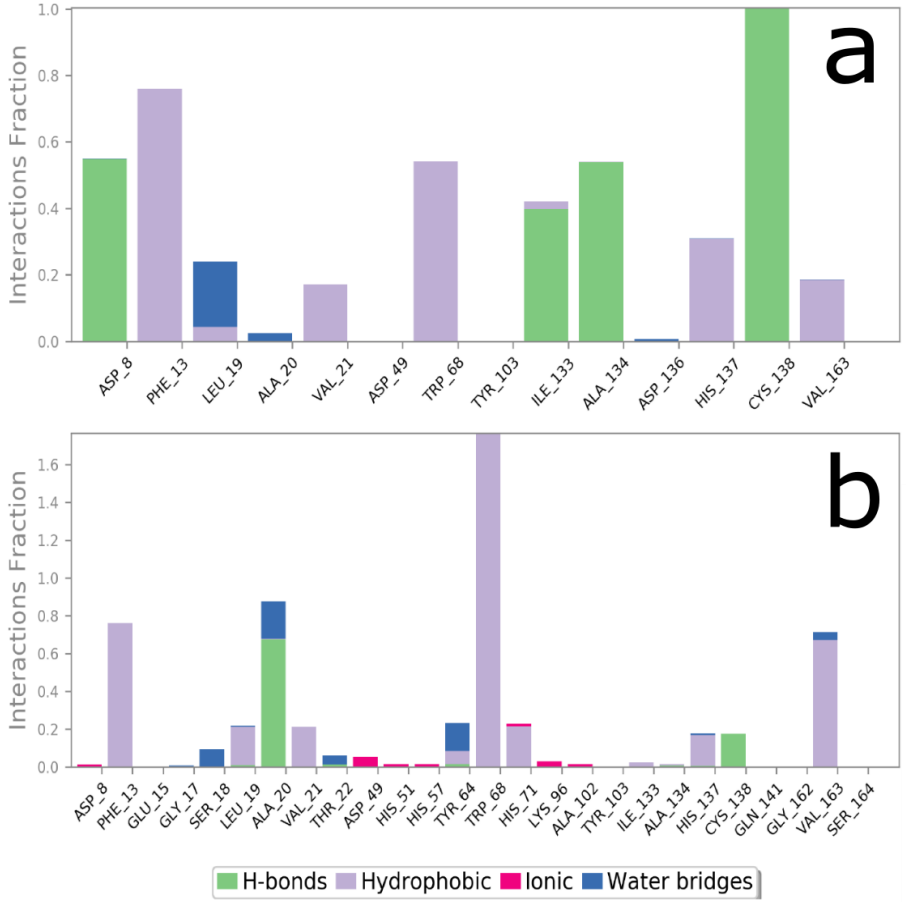

Figure 6. Fraction of interactions of the contact amino acids of PZase with **(a)** PZA and **(b)** C3.
Source: Elaborated by the authors.

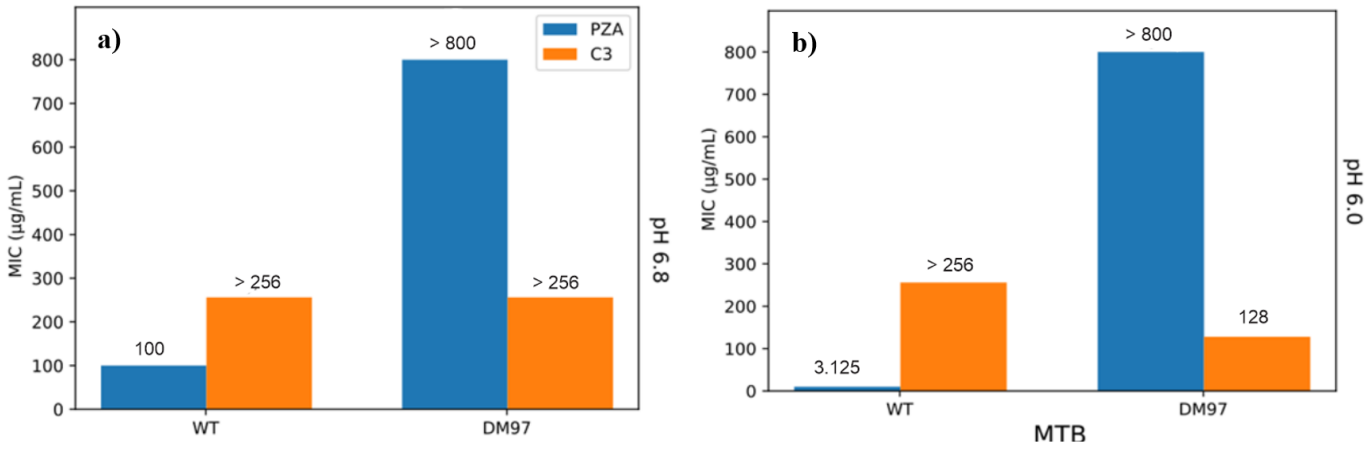

Figure 7. Minimum Inhibitory Concentration (MIC) of PZA and C3 at pH 6.8 **(a)** and 6.0 **(b)** for MTB H37Rv (WT) and DM97.
Source: Elaborated by the authors.

The MIC of C3 in DM97, at both pH levels, shows a lower concentration compared to PZA. According to docking and molecular dynamics studies, the C3-PZase and PZA-PZase systems are very similar, both in structural and energetic terms. Since the PZAase enzyme from H37Rv and DM97 is the same at the binding site, the improvement in MIC is not expected to be associated with this enzyme. Therefore, its greater chemical reactivity, liposolubility, polarity, and pKa, among others, may be decisive in its biochemical mechanism of action (Peterson *et al.*, 2015; Piddington *et al.*, 2000; Sun *et al.*, 2020; Zhang *et al.*, 2014).

Notably, the DM97 strain used in our study harbors the T135P mutation in the pyrazinamidase (PZase) enzyme, which is encoded by the pncA gene. This point mutation, located in proximity to the active site, has been associated with a complete loss of enzymatic activity, thereby preventing the conversion of PZA into its active form, pyrazinoic acid (POA). The T135P substitution likely alters the local structural flexibility required for nucleophilic attack during catalysis or disrupts substrate binding. As a result, DM97 exhibits high-level resistance to PZA, with an MIC greater than 800 µg/mL. Our findings confirm this phenotype and support the role of T135P as a critical determinant of resistance.

4. Conclusions

N'-[(1*E*)-(4-nitrophenyl)methylidene]pyrazine-2-carbohydrazide (C3) was prepared by a condensation between pyrazine-2-carbohydrazide with 4-nitrobenzaldehyde in 92% yield. The chemical characterization (UV-Vis, FT-IR, ^{1}H-NMR, and ^{13}C-NMR) allowed us to corroborate the proposed structure.

PZA-PZase and C3-PZase featured analogous dockings in both energy and pose. The difference occurs in the chemistry of C3, which exhibits greater chemical reactivity, liposolubility, and polarity, among other properties. On the other hand, *in vitro* studies revealed a lower MIC for MTB DM97 in C3 (MIC = 128 µg/mL at pH 6.0) compared to PZA (MIC > 800 µg/mL at pH 6.0). Being MTB DM97 resistant to PZA, this PZA-derived hydrazone sheds new light on the use of hydrazones for drug development associated with antimicrobial resistance.

Authors' contribution

Conceptualization: Christian Aliaga Paucar; Ana Valderrama Negrón; **Data curation:** Christian Aliaga Paucar; Jesús Alvarado Huayhuaz; Rocio Ramirez Panti; **Formal Analysis:** Christian Aliaga Paucar; Mirko Zimic Peralta; Patricia Sheen Cortavarria; Ana Valderrama Negrón; **Funding acquisition:** Ana Valderrama Negrón; **Investigation:** Christian Aliaga Paucar; Jesús Alvarado Huayhuaz; Henrry Gutierrez Vega; Rocio Ramirez Panti; Mirko Zimic Peralta; Patricia Sheen Cortavarria; Ana Valderrama Negrón; **Methodology:** Christian Aliaga Paucar; Jesús Alvarado Huayhuaz; Henrry Gutierrez Vega; Rocio Ramirez Panti; Mirko Zimic Peralta; Patricia Sheen Cortavarria; Ana Valderrama Negrón; **Project administration:** Ana Valderrama Negrón; **Resources:** Christian Aliaga Paucar; Ana Valderrama Negrón; **Software:** Christian Aliaga Paucar; Jesús Alvarado Huayhuaz; Rocio Ramirez Panti; **Supervision**: Mirko Zimic Peralta; Patricia Sheen Cortavarria; Ana Valderrama Negrón; **Validation:** Ana Valderrama Negrón; **Visualization**: Christian Aliaga Paucar; Jesús Alvarado Huayhuaz; Rocio Ramirez Panti; **Writing – original draft:** Christian Aliaga Paucar; Jesús Alvarado Huayhuaz; Rocio Ramirez Panti; **Writing – review & editing**: Mirko Zimic Peralta; Patricia Sheen Cortavarria; Ana Valderrama Negrón.

Conflict of interest

The authors declare that there is no conflict of interest.

Data availability statement

The data will be available upon request.

Artificial Intelligence usage statement

The authors declare that they did not use Artificial Intelligence tools at any stage of the preparation, correction, or evaluation of this work.

Funding

This work was funded by Management Agreement N° 237-2015-FONDECYT, to the Vicerrectorado de Investigación de la Universidad Nacional de Ingeniería Training Research Project 2019 code: FC-MF-1-2019.

Acknowledgments

We are grateful to Dr. Maribel Navarro Acosta (Biometallodrugs and Catalysis Chemistry Laboratory, Juiz de Fora, Minas Gerais, Brazil) for registering the Nuclear Magnetic Resonance spectra and elemental analysis. We thank Professor Dr. Breno Pannia Esposito for his valuable review and suggestions to manuscript, Professor Dr. Ataualpa Alberto Carmo Braga, for his academic support and facilities provided for the use of Heimdall supercomputer from Institute of Chemistry of Sao Paulo University, Brazil. We also thank the High Computational Performance Center of the Instituto de Investigaciones de la Amazonía del Perú (IIAP), Eng. Isaac Ocampo Yahuarcani and Eng. Rodolfo Cárdenas Vigo, for their support in the use of the Manati supercomputer.

References

Abdel-Aziz, M.; Abdel-Rahman, H. M. Synthesis and anti-mycobacterial evaluation of some pyrazine-2-carboxylic acid hydrazide derivatives. *Eur. J. Med. Chem.* **2010**, *45* (8), 3384–3388. https://doi.org/10.1016/j.ejmech.2010.04.025

Allouche, A. R. Gabedit—A graphical user interface for computational chemistry software. *J. Comput. Chem.* **2011**, *32* (1),174–182. https://doi.org/10.1002/jcc.21600

Alvarado-Huayhuaz, J. A.; Talaverano-Rojas, D. A.; Huamán Quispe, R. I.; Dorneles Caldeira Balboni, M.; Arrúa Arce, O. E.; Velasque Werhli, A.; Santos Machado, K.; Valderrama-Negrón, A. C. Search for Zinc Complexes with High Affinity in Pyrazinamidase from Mycobacterium Tuberculosis Resistant to Pyrazinamide. In: Scherer, N. M.; Melo-Minardi, R. C. Eds.; Advances in Bioinformatics and Computational Biology; *BSB 2022. Lecture Notes in Computer Science.* Springer; **2022**, 13523. https://doi.org/10.1007/978-3-031-21175-1_12

Benov, L. Effect of growth media on the MTT colorimetric assay in bacteria. *PLoS One*. **2019**, *14* (8), e0219713. https://doi.org/10.1371/journal.pone.0219713

Bhaskar, R. S.; Ladole, C. A.; Salunkhe, N. G.; Barabde, J. M.; Aswar, A. S. Synthesis, characterization and antimicrobial studies of novel ONO donor hydrazone Schiff base complexes with some divalent metal (II) ions. *Arab. J. Chem.* **2019**, *13* (8), 6559–6567. https://doi.org/10.1016/j.arabjc.2020.06.012

Bowers, K. J.; Chow, D. E.; Xu, H.; Dror, R. O.; Eastwood, M. P.; Gregersen, B. A.; Klepeis, J. L.; Kolossvary, I.; Moraes, M. A.; Sacerdoti, F. D. Scalable algorithms for molecular dynamics simulations on commodity clusters. In *SC'06: Proceedings of the 2006 ACM/IEEE Conference on Supercomputing*. **200**6, pp. 43–43. IEEE. https://doi.org/10.1145/1188455.1188544

Carrasco, F.; Hernández, W.; Chupayo, O.; Sheen, P.; Zimic, M.; Coronel, J.; Álvarez, C. M.; Ferrero, S. Oramas-Royo, S.; Spodine, E. Phenylisoxazole-3/5-Carbaldehyde Isonicotinylhydrazone derivatives: Synthesis, Characterization, and Antitubercular Activity. *J. Chem*. **2021**, *2021* (1), 1–14. https://doi.org/10.1155/2021/6014093

Chávez, N.; Ramírez, R.; Sheen, P.; Zimic, M.; Valderrama, A. Síntesis, caracterización y evaluación de la actividad biológica de compuestos de coordinación de cobalto con pirazinamida. *Rev. Soc. Quím. Perú.* **2020**, *86* (3), 315–328. https://doi.org/10.37761/rsqp.v86i3.303

Daina, A.; Michielin, O.; Zoete, V. SwissADME: a free web tool to evaluate pharmacokinetics, drug-likeness and medicinal chemistry friendliness of small molecules. *Sci. Rep.* **2017**, *7* (1), 42717. https://doi.org/10.1038/srep42717

Dogan, H.; Dogan, Ş. D.; Gunduz, M. G.; Krishna, V. S.; Sarıpınar, E. Discovery of hydrazone containing thiadiazoles as Mycobacterium tuberculosis growth and enoyl acyl carrier protein reductase (InhA) inhibitors. *Eur. J. Med. Chem.* **2020**, *188*, 112035. https://doi.org/10.1016/j.ejmech.2020.112035

Ferreira, M.; Candea, A. L.; O Henriques, G. M.; Kaiser, C. R.; Lima, C. H. S.; Souza, M. V. Synthesis and cytotoxic evaluation of disubstituted N-acylhydrazones pyrazinecarbohydrazide derivatives. *Lett. Drug Des. Discov.* **2010**, *7* (4), 275–280. https://doi.org/10.2174/157018010790945814

Hanwell, M. D.; Curtis, D. E.; Lonie, D. C.; Vandermeersch, T.; Zurek, E.; Hutchison, G. R. Avogadro: an advanced semantic chemical editor, visualization, and analysis platform. *J. Cheminform.* **2012**, *4* (1), 17. https://doi.org/10.1186/1758-2946-4-17

Hegde, G. S.; Netalkar, S. P.; Revankar, V. K. Copper (II) complexes of 3,5-di-tert-butyl-2-hydroxybenzoylhydrazones of 2-formylpyridine and 2-acetylpyridine, with tautomeric azine-scaffold-based architecture: Synthesis, crystal structures, the effect of counteranions on complexation, and their anti-microbial and anti-tuberculosis evaluation. *Appl. Organomet. Chem.* **2019**, *33* (7), e4840. https://doi.org/10.1002/aoc.4840

Instituto de Investigaciones de la Amazonía Peruana (IIAP). Centro de Alto Rendimiento Computacional de la Amazonia Peruana. Systèmes D., "BIOVIA." San Diego, 2020.

Jorgensen, W. L.; Chandrasekhar, J.; Madura, J. D.; Impey, R. W.; Klein, M. L. Comparison of simple potential functions for simulating liquid water. *J. Chem. Phys.* **1983**, *79* (2), 926–935. https://doi.org/10.1063/1.445869

Junaid, M.; Khan, M. T.; Malik, S. I.; Wei, D. Q. Insights into the mechanisms of the pyrazinamide resistance of three pyrazinamidase mutants N11K, P69T, and D126N. *J. Chem. Inf. Model.* **2019**, *59* (1), 498–508. https://doi.org/10.1021/acs.jcim.8b00525

Kardan-Yamchi J.; Kazemian, H.; Battaglia, S.; Abtahi, H.; Rahimi, F. A.; Hamzelou, G.; Cirillo, D. M.; Ghodousi, A.; Feizabadi, M. M. Whole Genome Sequencing Results Associated with Minimum Inhibitory Concentrations of 14 Anti-Tuberculosis Drugs among Rifampicin-Resistant Isolates of Mycobacterium Tuberculosis from Iran. *J. Clin. Med.* **2020**, *9* (2), 465. https://doi.org/10.3390/jcm9020465

Lee, C.; Yang, W.; Parr, R. G. Development of the Colle-Salvetti correlation-energy formula into a functional of the electron density. *Phys. Rev. B*. **1988**, *37* (2), 785. https://doi.org/10.1103/PhysRevB.37.785

Liu, Y.; Peterson, D. A.; Kimura, H; Schubert, D. Mechanism of cellular 3-(4, 5-dimethylthiazol-2-yl)-2, 5-diphenyltetrazolium bromide (MTT) reduction. *J. Neurochem*. **1987**, *69* (2), 581–593. https://doi.org/10.1046/j.1471-4159.1997.69020581.x

Ministry of Health of Peru (MINSA), Perfil de la tuberculosis en el Perú. 2019. [Online]. Available: https://www.dge.gob.pe/portal/docs/tools/teleconferencia/2022/SE272022/03.pdf. (accessed 2023-01-19).

Neese, F. Software update: the ORCA program system, version 4.0. *Wiley Interdiscip. Rev. Comput. Mol. Sci.* **2018**, *8* (1), e1327. https://doi.org/10.1002/wcms.1327

Peterson, N. D.; Rosen, B. C.; Dillon, N. A.; Baughn, A. D. Uncoupling Environmental pH and Intrabacterial Acidification from Pyrazinamide Susceptibility in Mycobacterium tuberculosis. *Antimicrob. Agents Chemother.* **2015**, *59* (12), 7320–7326. https://doi.org/10.1128/AAC.00967-15

Petrella, S.; Gelus-Zietal, N.; Maudry, A.; Laurans, C.; Boudjelloul, R.; Sougakoff, W. Crystal Structure of the Pyrazinamidase of *Mycobacterium tuberculosis*: Insights into Natural and Acquired Resistance to Pyrazinamide. *PLoS ONE*. **2011**, *6* (1). e15785. https://doi.org/10.1371/journal.pone.0015785

Piddington, D. L; Kashkouli, A.; Buchmeier, N. A. Growth of Mycobacterium tuberculosis in a Defined Medium Is Very Restricted by Acid pH and Mg^{2+} Levels. *Infect. Immunity*. **2000**, *68* (8), 4518–4522. https://doi.org/10.1128/IAI.68.8.4518-4522.2000

Schrödinger Release, 2022-2: Induced Fit Docking protocol; Glide, Schrödinger, LLC, New York, NY, 2021; Prime, Schrödinger, LLC, New York, NY, 2021. Available: https://www.schrodinger.com/products/glide (accessed 2022-06-12).

Shebl, M. Coordination behavior of new bis(tridentate ONO, ONS and ONN) donor hydrazones towards some transition metal ions: Synthesis, spectral, thermal, antimicrobial and antitumor studies. *J. Mol. Struct.* **2017**, *1128*, 79–93. https://doi.org/10.1016/j.molstruc.2016.08.056

Shebl, M.; Saleh, A. A.; Khalil, S. M.; Dawy, M.; Ali, A. A. Synthesis, spectral, magnetic, DFT calculations, antimicrobial studies and phenoxazinone synthase biomimetic catalytic activity of new binary and ternary Cu(II), Ni(II) and Co(II) complexes of a tridentate ONO hydrazone ligand. *Inorg. Nano-Met. Chem.* **2020**, *51* (2), 195–209. https://doi.org/10.1080/24701556.2020.1770794

Sheen, P.; Lozano, K.; Gilman, H.; Valencia, J.; Loli, S.; Fuentes, P.; Zimic, M. *pncA* gene expression and prediction factors on pyrazinamide resistance in Mycobacterium tuberculosis. *Tuberculosis*. **2013**, *93* (5), 515–522. https://doi.org/10.1016/j.tube.2013.03.005

Silva, Y. K. C.; Augusto, C. V.; Castro, M. L.; Albuquerque, G. M.; de Queiroz, A. C.; Dias, D. F.; Alexandre-Moreira, M. S. Synthesis and pharmacological evaluation of pyrazine N-acylhydrazone derivatives designed as novel analgesic and anti-inflammatory drug candidates. *Bioorg. Med. Chem.* **2010**, *18* (14), 5007–5015. https://doi.org/10.1016/j.bmc.2010.06.002

Singh, P.; Mishra, A. K.; Malonia, S. K.; Chauhan, D. S.; Sharma, V. D.; Venkatesan, K.; Katoch, V. M. The paradox of pyrazinamide: an update on the molecular mechanisms of pyrazinamide resistance in Mycobacteria. *J. Commun. Dis.* **2006**, *38* (3), 288.

Srivastava, G.; Darokar, M. P; Sharma, A. Molecular investigation against the resistant mechanism of PncA mutated pyrazinamide resistance and insight into the role of pH environment for pyrazinamide activation. *J. Biomol. Struct. Dyn.* **2019**, *38* (11), 3411–3431. https://doi.org/10.1080/07391102.2019.1659854

Sun, Q.; Li, X.; Perez, M.; Shi, W.; Zhang, Y.; Sacchettini, C. The molecular basis of pyrazinamide activity on Mycobacterium tuberculosis PanD. *Nat. Commun*. **2020**, *11* (1), 339. https://doi.org/10.1038/s41467-019-14238-3

Supo-Escalante, R. R.; Médico, A.; Gushiken, E.; Olivos-Ramírez, G. E.; Quispe, Y.; Torres, F.; Zimic, M. Prediction of Mycobacterium tuberculosis pyrazinamidase function based on structural stability, physicochemical and geometrical descriptors. *Plos One*. **2020**, *15* (7), e0235643. https://doi.org/10.1371/journal.pone.0235643

Tariq, S.; Khalid, M.; Raza, A. R.; Rubab, S. L.; Alcântara Morais, S. F.; Khan, M. U.; Braga, A. C. Experimental and computational investigations of new indole derivatives: A combined spectroscopic, SC-XRD, DFT/TD-DFT and QTAIM analysis. *J. Mol. Struct.* **2020**, *1207*, 127803. https://doi.org/10.1016/j.molstruc.2020.127803

Valderrama Negrón, A. C.; Ramirez Panti, R. I.; Aliaga Paucar, C. M.; Grandez Arias, F.; Sheen Cortovaria, P.; Zimic Peralta, M. J.; Cauna Orocollo, Y. Pyrazinamide-isoniazid hybrid: synthesis optimisation, characterisation, and antituberculous activity. *Rev. Colomb. Quim.* **2021**, *50* (3), 16–23. https://doi.org/10.15446/rev.colomb.quim.v50n3.96424

Vergara, F. M.; Lima, C. D.; Maria, M. D.; Candéa, A. L.; Lourenço, M. C.; Ferreira, M. D.; Souza, M. V. Synthesis and antimycobacterial activity of N′-[(E)-(monosubstituted-benzylidene)]-2-pyrazinecarbohydrazide derivatives. *Eur. J. Med. Chem.* **2009**, *44* (12), 4954–4959. https://doi.org/10.1016/j.ejmech.2009.08.009

Wang, Z. N'-(2-Hydroxy-3-methoxybenzylidene)pyrazine-2-carbohydrazide monohydrate. *IUCrDATA*. **2020**, *5* (1), x191731. https://doi.org/10.1107/S2414314619017310

World Health Organization (WHO). Global tuberculosis report. 2023. [Online]. Available: https://www.who.int/teams/global-programme-on-tuberculosis-and-lung-health/tb-reports/global-tuberculosis-report-2023 (accessed 2023-01-08).

Zhang, Y.; Shi, W.; Zhang, W.; Mitchison, D. Mechanisms of pyrazinamide action and resistance. *Microbiol Spectr.* **2014**, *2* (4), 2–4. https://doi.org/10.1128/microbiolspec.MGM2-0023-2013

Zhang, Y.; Wade, M.; Scorpio, A.; Zhang, H.; Sun, Z. Mode of action of pyrazinamide: disruption of Mycobacterium tuberculosis membrane transport and energetics by pyrazinoic acid. *J. Antimicrob. Chemother.* **2003**, *52* (5), 790–795. https://doi.org/10.1093/jac/dkg446

Zülfikaroğlu, A.; Yüksektepe, Ç.; Çelikoğlu, E.; Çelikoğlu, U.; İdil, Ö. New Cu(II), Co(III) and Ni(II) metal complexes based on ONO donor tridentate hydrazone: Synthesis, structural characterization, and investigation of some biological properties. *J. Mol. Struct.* **2020**, *1199,* 127012. https://doi.org/10.1016/j.molstruc.2019.127012

https://doi.org/10.26850/1678-4618.eq.v51.2026.e1506

Supplementary Information

According to the C3 microspecies distribution analysis, the neutral species predominates at pH 7.4.

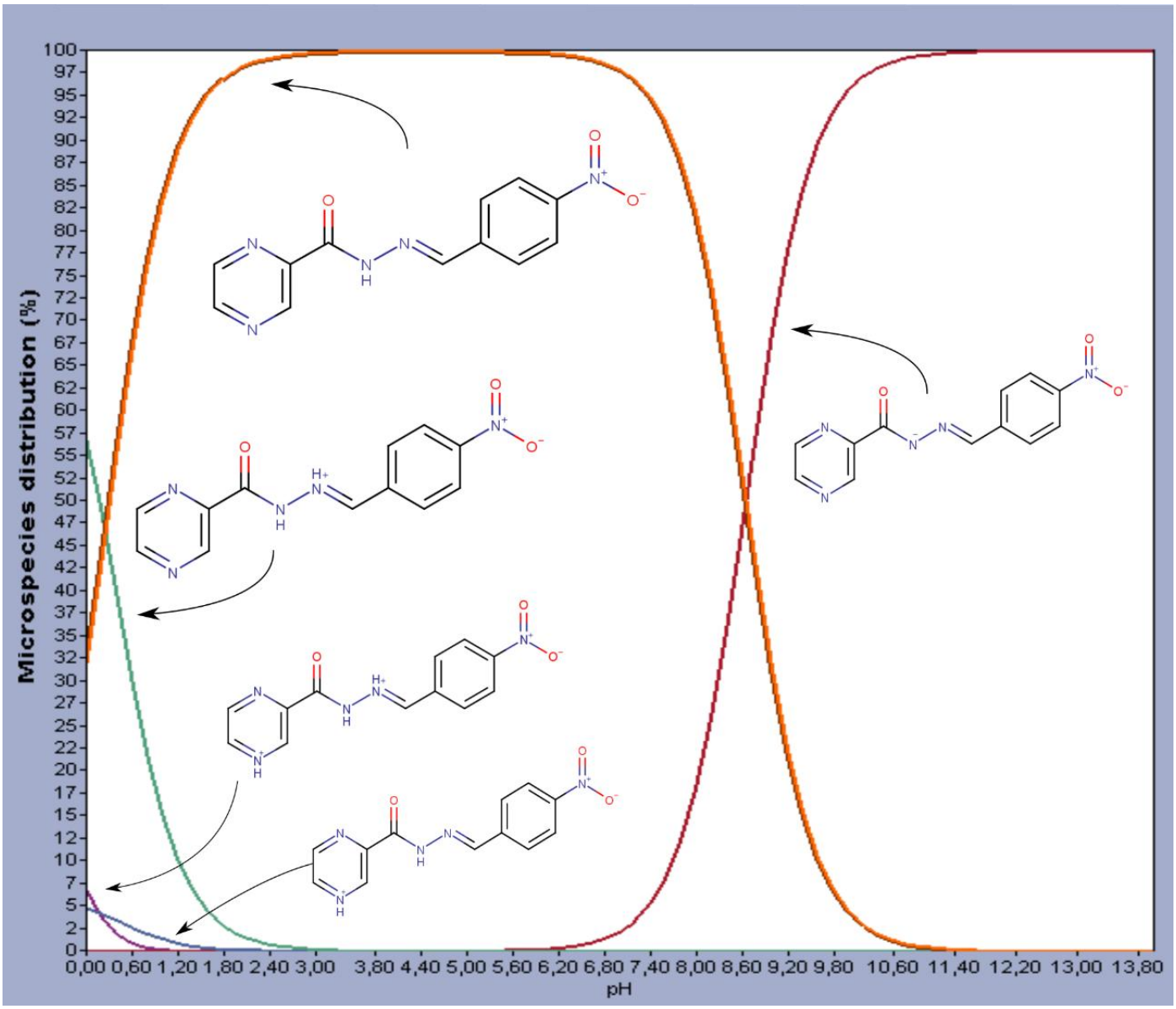

Figure 1S. Percentage of distribution of microspecies of C3 according to pH.
Source: Elaborated by the authors.

[1]H-NMR spectrum of compound C3.

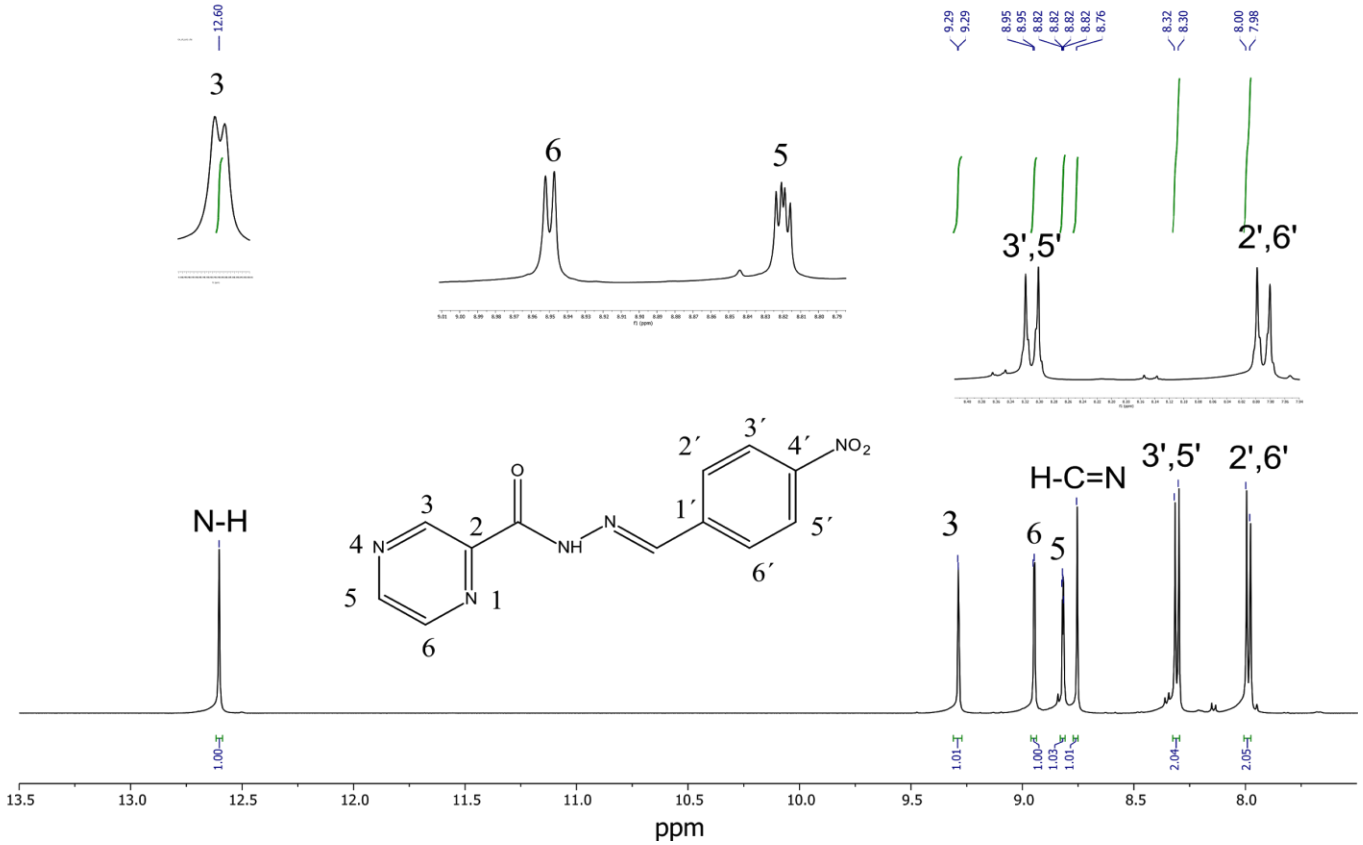

Figure 2S. [1]H-NMR spectrum of compound C3 (DMSO-d_6, 500 MHz).
Source: Elaborated by the authors.

[13]C-NMR spectrum of compound C3.

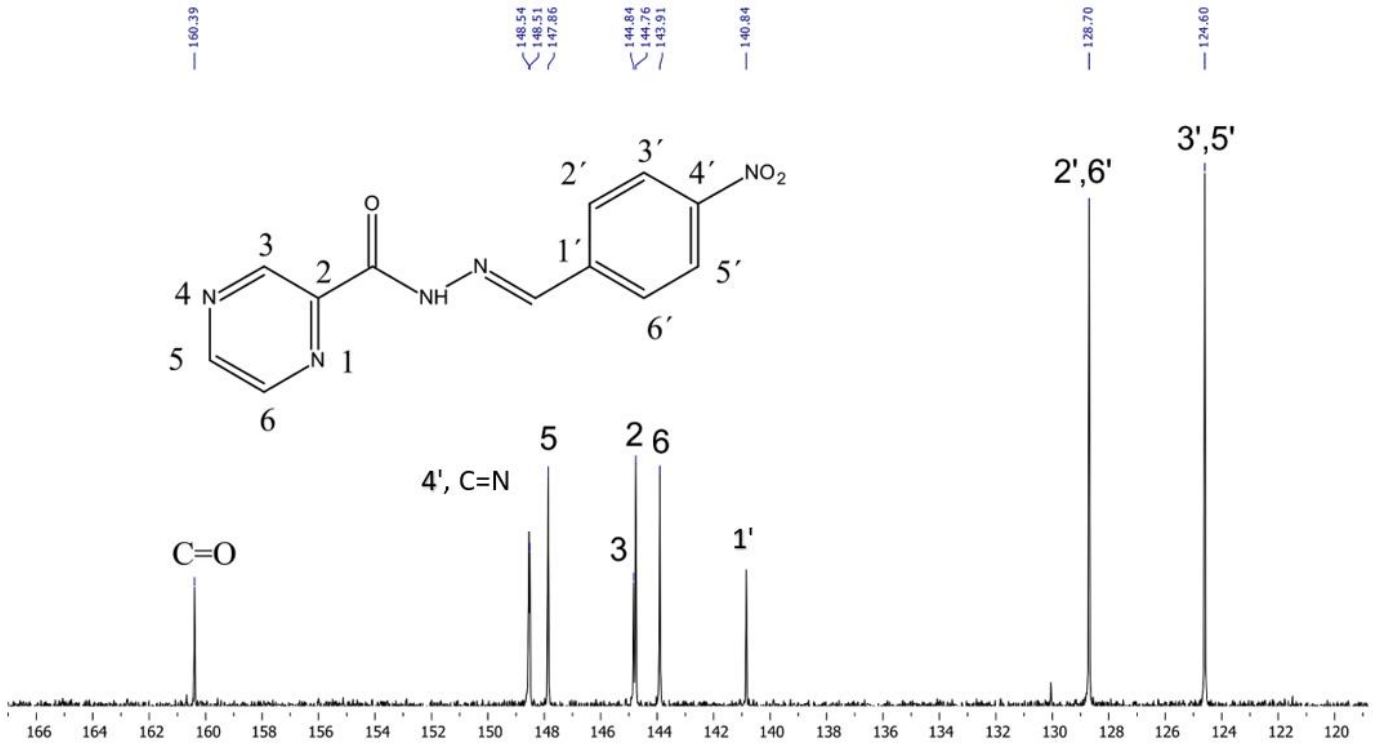

Figure 3S. [13]C-NMR spectrum of compound C3 (DMSO-d_6, 500 MHz).
Source: Elaborated by the authors.

The Bioavailability radar shows six physicochemical properties:

(1) Lipophilicity: XLOGP3 between −0.7 and +5.0, (2) size: MW between 150 and 500 g/mol, (3) polarity: TPSA between 20 and 130 $Å^2$, (4) solubility: logS not higher than 6, (5) saturation: fraction of carbons in the sp3 hybridization not less than 0.25, and (6) flexibility: no more than 9 rotatable bonds.

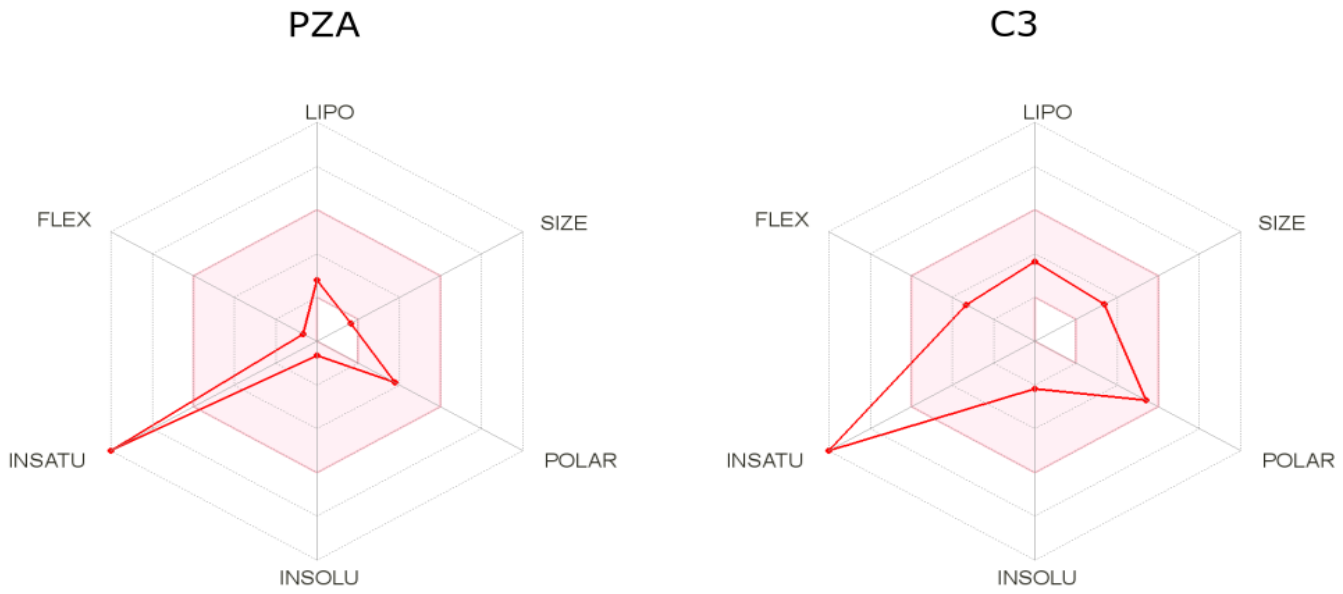

Figure 4S. Bioavailability radar for PZA and C3. Values in the pink area are recommended to predict oral bioavailability according to SwissADME.

Source: Elaborated by the authors.